Published in final edited form as:
Nat Nanotechnol. 2010 January ; 5(1): 42–47. doi:10.1038/nnano.2009.314.

Design Considerations for Tumor-Targeted Nanoparticles

Hak Soo Choi[1], **Wenhao Liu**[2], **Fangbing Liu**[1], **Khaled Nasr**[1], **Preeti Misra**[1], **Moungi G. Bawendi**[2], and **John V. Frangioni**[1,3,*]

[1]Division of Hematology/Oncology, Department of Medicine, Beth Israel Deaconess Medical Center, Boston, MA 02215

[2]Department of Chemistry, Massachusetts Institute of Technology, Cambridge, MA 02139

[3]Department of Radiology, Beth Israel Deaconess Medical Center, Boston, MA 02215

Abstract

DIAGNOSTIC AGENTS—Nanoparticles functionalized with ligands that target tumors can be cleared from the body through the kidneys if they have a hydrodynamic diameter of less than 5.5 nm.

Keywords

Nanotechnology; Quantum Dots; Nanoparticles; Diagnostic Imaging; Image-Guided Surgery; Biodistribution; Clearance; Fluorescence Imaging; Tumor Targeting

INTRODUCTORY PARAGRAPH

Inorganic/organic hybrid nanoparticles are potentially useful in biomedicine but to avoid non-specific background fluorescence and long-term toxicity, they need to be cleared from the body within a reasonable time scale.[1] Previously, we showed that rigid spherical nanoparticles such as quantum dots can be cleared by the kidneys if they had a hydrodynamic diameter less than 5.5 nm and a zwitterionic surface charge.[2] Here we show that quantum dots functionalized with high-affinity small molecule ligands that target tumors can also be cleared by the kidneys if their hydrodynamic diameter is less than this value, which sets an upper limit of 5-10 ligands per quantum dot for renal clearance. Animal models of prostate cancer and melanoma show receptor-specific imaging and renal clearance within 4 h post-injection. This study suggests a set of design rules for the clinical translation of targeted nanoparticles that can be eliminated through the kidneys.

Although many classes of biocompatible, inorganic-based nanomaterials have been developed for medical diagnostics and therapeutics,[3-7] many presently available formulations require potentially toxic elements.[8] Efforts have been made to reduce toxicity by modulating the composition, particle shape, physical size, and surface coating of the nanoparticles.[9] One common strategy is to engineer nanoparticles using biocompatible and biodegradable polymeric coatings.[10-13] However, polymer coatings generally increase particle size over the

*Corresponding Author: John V. Frangioni, M.D., Ph.D., Beth Israel Deaconess Medical Center, 330 Brookline Avenue, Room SL-B05, Boston, MA 02215, Phone: 617-667-0692 Fax: 617-667-0981, jfrangio@bidmc.harvard.edu

Author contributions

H.S.C., W.L., F.L., K.N., and P.M. performed the experiments. H.S.C., M.G.B., and J.V.F. reviewed, analyzed, and interpreted the data. H.S.C., M.G.B., and J.V.F. wrote the paper. All authors discussed the results and commented on the manuscript.

Competing financial interests

The authors declare no competing financial interests.

desired range, which can result in nonspecific background, long circulation times, and accumulation over time into the reticuloendothelial system (RES; i.e., liver, spleen, lymph nodes, and bone marrow).[12,14] In addition, polymer coatings may activate inflammatory or immunological responses,[15] and the degradation of polymer coatings leads to exposure of inorganic surfaces, which can do the same.[16,17]

Clinical translation of nanotechnology will require nanoparticles with the lowest possible likelihood of toxicity. One important strategy to minimize toxicity is to remove all unbound material completely from the body, that is, excrete it via the liver (into bile) or via the kidneys (into urine). Whereas hepatic clearance is unpredictable and variable,[18,19] renal excretion tends to follow predictable rules.[2] Yet, to date, there have not been any nanoparticles described that can target a disease state, as well as be cleared efficiently from the body in a reasonable amount of time.

In 2004, Gao *et al.*[4] reported a landmark paper on *in vivo* cancer targeting with semiconductor quantum dots, and since that time numerous additional papers on this topic have been published.[20-23] However, most of these papers fail to consider the autofluorescence of living tissue, the passive targeting caused by leaky tumor vasculature, the use of a receptor-negative tumor as a control, and the high background accumulation of nanoparticles in the RES. Indeed, most tumor targeting of nanoparticles in animals described to date is likely the result of enhanced permeability and retention,[24] and not specific targeting.

To render nanoparticles viable for clinical translation, it is necessary to understand the key design considerations that govern their behavior *in vivo*. Starting with ultrasmall, zwitterionic quantum dots (QDs) previously described by our group[2] as a model system, we hypothesized that it should be possible to define the ligand properties, ligand conjugation ratio, hydrodynamic diameter (HD), and surface characteristics that permit tumor-specific targeting in a living system, and to develop targeted nanoparticles that are eliminated completely from the body if not bound to the desired tumor.

To demonstrate the generality of the technology, we developed two different types of QDs, one targeting prostate-specific membrane antigen (PSMA)-positive prostate cancer cells via the small molecule ligand GPI,[25] and one targeting integrin $\alpha_v\beta_3$-positive melanoma cells via the small molecule cRGD.[26] We prepared ultrasmall CdSe(ZnCdS) core(shell) nanocrystals that were rendered aqueous-soluble with a zwitterionic cysteine coating (Fig. 1a),[2,27] while retaining a reasonably high quantum yield (28%). To minimize the impact of tissue autofluorescence and to improve *in vivo* detectability, we conjugated ≈1.4 molecules of the organic NIR fluorophore IRDye™800-CW to each visibly fluorescent QD (QD-CW) prior to ligand conjugation. Finally, high-affinity small molecule targeting ligands were conjugated covalently to the carboxylic groups of the QD surface using standard carbodiimide chemistry to form QD-CW-GPI or QD-CW-cRGD (see Supplementary Methods). Although the cysteine-coated core(shell) nanocrystals were small enough to be excreted via the kidneys, the number of conjugated ligands needed to be limited such that the overall HD was ≈5.5 nm, which is approximately the threshold for rapid renal excretion at 4 h post-injection.[2] Using HD as measured by gel-filtration chromatography, we determined that only 5 to 10 GPI or cRGD small molecules could be conjugated to the QD-CW surface while still maintaining the small HD needed for renal clearance (Fig. 1b). Importantly, though, QD-CW-GPI and QD-CW-cRGD ligand prepared in this way did not show any binding to serum proteins, which would lead to a further increase in HD (see Supplementary Methods).[2]

The specificity of QD-CW-GPI and QD-CW-cRGD binding to the surface of living cancer cells was confirmed using human prostate cancer and melanoma cell lines. As shown in Fig. 2, QD-CW-GPI bound to PSMA-positive LNCaP human prostate cancer cells, but not to

PSMA-negative PC-3 human prostate cancer cells. Similarly, QD-CW-cRGD showed significant binding to $\alpha_v\beta_3$-positive M21 human melanoma cells, but not to $\alpha_v\beta_3$-negative M21-L human melanoma cells.

To quantify QD biodistribution, blood levels, and clearance from the body, QDs were labeled with ^{99m}Tc (Supplementary Methods and Fig. 3) and injected intravenously. The measured β-phase blood half-lives ($t_{1/2\beta}$) of ^{99m}Tc-QD-GPI and ^{99m}Tc-QD-cRGD were extremely similar, being 126 min and 113 min, respectively. At 4 h post-injection, organs and tumors were resected and activities were measured. The most intense uptakes for ^{99m}Tc-QD-GPI were measured in the liver (9.6 ± 3.8 %ID), kidneys (5.1 ± 3.0 %ID), and intestine (1.9 ± 1.8 %ID) (Fig. 3a), consistent with active excretion. Similarly, the remaining activity of ^{99m}Tc-QD-cRGD was found in the liver (10.2 ± 5.7 %ID), kidneys (6.5 ± 2.5 %ID), and intestine (4.4 ± 3.2 %ID) (Fig. 3b). Importantly, over 65% of the ligand-targeted QDs were completely eliminated by the body within 4 h post-injection, appearing primarily in the urine (Fig. 3c). At 24 h post-injection, total carcass retention was ≈9% for both targeted QDs (data not shown).

In vivo tumor targeting, biodistribution, and clearance of targeted QDs were demonstrated using NIR fluorescence imaging. As shown in Fig. 4a, a large amount of QD-CW-GPI accumulated in the LNCaP tumor site (PSMA-positive) over 4 h. The positive- to negative-tumor ratio was 2.8 and the tumor-to-background ratio was 5.0. Cross-sectional imaging revealed that QD uptake into solid tumors displayed expected variability, with some tumors showing homogeneous uptake and others showing less homogenous uptake (see Supplementary Methods). Most of the remaining QDs were excreted through renal filtration and were found primarily in the bladder (Fig. 4a, Supine). Fluorescence imaging revealed that apart from the kidneys and bladder, most tissues and organs had extremely low levels of fluorescence (Fig. 4b). We further validated the tumor targeting and background-clearing properties of our QDs using the cRGD/integrin system. Tumor accumulation was high, with a positive- to negative-tumor ratio of 5.1 and a tumor-to-background ratio of 6.9. Once again, excretion was primarily renal, with most of the injected dose appearing in the urine (Fig. 4c,d). Confirming these results, urine collected 4 h post-injection of QD-CW-GPI and QD-CW-cRGD was highly fluorescent, and had a gel-filtration chromatography pattern very similar to QDs in PBS (Fig. 5).

There are three major challenges with using nanoparticles as *in vivo* diagnostics and therapeutics: 1) high background retention in the RES, 2) lack of complete elimination from the body, and 3) arriving at an HD small enough for rapid equilibration between the intravascular and extravascular spaces. Solving all of these problems, while maintaining high specificity for desired targets, is extremely difficult. In previous work, we demonstrated that an HD ≤ 5.5 nm was required for efficient renal clearance of spherical nanoparticles.[2] In the present study, we show that it is indeed possible to target renally-cleared QDs to tumors, but the HD increase due to the targeting ligand(s) is severely limiting. Only 5 to 10 small molecule ligands could be conjugated to the surface of QDs before the increased HD precluded rapid renal clearance. Nevertheless, using this strategy, the majority of the injected, unbound dose was excreted by 4 h, while receptor-specific targeting was preserved. Interestingly, the ability to control the number of targeting ligands on the QD surface while maintaining renal clearance preserves the option of using "multiplexed" targeting. That is, it should be possible to conjugate two (or more) different targeting ligands to the QD surface to more effectively target tumors that express multiple receptor types.[4,28]

With many inorganic/organic hybrid nanoparticle systems, it remains a challenge to generate a final HD of ≈5.5 nm.[29] The nanocrystals used in this study might actually represent a worst-case scenario, since the organic NIR fluorophore molecule occupies surface area that could have otherwise been used for a small molecule targeting ligand. Our data may also be applicable

to larger nanoparticles, provided that they degrade to renally-filterable metabolites. If degradation occurs before uptake by the RES, renal elimination should be efficient, even if the degradation products contain targeting ligands.[17] The only caveat is surface charge, and thus, the charge to HD ratio. Highly anionic or cationic QDs and their fragments have a tendency to bind serum proteins and increase their HD.[2] This is one of the key reasons why we began with a zwitterionic surface coating and were careful to minimize the number of anionic targeting ligands, such as GPI and cRGD, conjugated to this coating.

Finally, the desired HD of ≈5.5 nm is for "rapid" renal clearance, i.e., the majority of the dose being eliminated by 4 h. Four hours is chosen as the key imaging time because it is "clinically realistic" for human surgery. For example, the dose could be given as soon as the patient arrives in the pre-op area, thus providing an imaging window that would last for several hours during image-guided surgery.[30] For nanoparticles with an HD slightly larger than the threshold, it might still be possible to eliminate them in urine, but longer clearance times would be necessary.

We report the rules for designing tumor-targeted nanoparticles for *in vivo* imaging that can be renally cleared using QDs as a model particle. We hope this study will lay the foundation for designing targeted nanoparticles with the optimal composition, particle size, and surface coating to control biodistribution, elimination from the body, and receptor-based targeting. Finally, elimination in urine helps negate concerns over toxicity, thus making clinical translation more viable.

METHODS

Synthesis of QD-CW-GPI and QD-CW-cRGD

Aqueous-soluble, cysteine-coated CdSe(ZnCdS) core(shell) nanocrystals with a HD of 3.4 nm were synthesized according to previous studies.[2,27] Near-infrared fluorophore IRDye800-CW (LI-COR, Lincoln, NE) was conjugated covalently to the QD surface (QD-CW) in PBS, pH 7.8 to a labeling ratio of 1.4. QD-CW was resuspended in 0.1 M 2-(N-morpholino) ethanesulfonic acid (MES) at pH 6, and treated with carbodiimide 1-ethyl-3-(3-dimethyllaminopropyl)carbodiimide (EDC; Pierce) and sulfo-NHS (Pierce). The suspension was incubated for 15 min, and excess reagents removed by ultrafiltration. GPI (2-[((3-amino-3-carboxypropyl)(hydroxy)phosphinyl)-methyl]pentane-1,5-dioic acid)[25] or cRGD (monomeric cyclic Arg-Gly-Asp peptide)[26] was dissolved in PBS, pH 8.0, and mixed with the MES solution. After a 3 h reaction, the mixtures were subjected to ultrafiltration with Tris (pH 8.0) to remove any unconjugated dye and to quench unreacted NHS ester. The labeling ratio was determined by UV-Vis absorption measurements (labeling ratio = 5 - 10). See Supplementary Methods for detailed experimental methods.

Gel-filtration chromatography

Details of the custom chromatography system, which permits on-line, full-spectrum analysis of QD absorbance and fluorescence, have been published previously.[30] Calibration of HD was performed by injecting 100 μL of protein standards containing γ-globulin (M1, 158 kDa, 11.9 nm HD), ovalbumin (M2, 44 kDa, 6.13 nm HD), myoglobin (M3, 17 kDa, 3.83 nm HD), and vitamin B_{12} (M4, 1.35 kDa, 1.48 nm HD). All HD measurements were performed with three independent experiments. For measurement of the effects of serum protein adsorption, 2.5 μM QDs were incubated in PBS or 100% mouse serum for 4 h at 37°C prior to loading 100 μL onto the column.

In vitro cell binding studies

The human prostate cancer cell lines LNCaP (ATCC, Manassas, VA) and PC-3 (ATCC, Manassas, VA) were cultured in Dulbecco's Modified Eagle's Medium (DMEM, Mediatech, Hermdon, VA), supplemented with 10% FBS and 5% penicillin/streptomycin under a 5% carbon dioxide atmosphere. Human M21 and M21-L melanoma cells were grown in RPMI 1640 (Mediatech, Hermdon, VA). Cells were seeded onto sterilized 18-mm-diameter glass coverslips in 12-well plates (3×10^5 cells per well), and incubated overnight at 37°C. Cells were then washed with PBS and incubated in pre-cooled, serum-containing medium at 4°C in the presence of 0.5 μM QD-CW-GPI or 1 μM QD-CW-cRGD for 30 min. They were then washed with PBS and fixed with 2% paraformaldehyde at room temperature for 10 min. The slides were observed on a previously described four-channel NIR fluorescence microscope.[25]

Intraoperative fluorescence imaging of tumor-bearing mice

An intraoperative fluorescence imaging system optimized for animal surgery has been described in detail previously.[30] For fluorescence excitation, LEDs (Marubeni Epitex, New York, NY) fitted with 760 ± 20 nm (NIR) or 470 ± 20 nm (blue) excitation filters in custom holders were used. The emission filter was a 795 nm long pass. Exposure time (200 ms) and normalizations were the same for all fluorescence images. Color video was collected on a separate optical channel using computer-controlled camera acquisition via custom LabVIEW software (National Instruments, Austin, TX).

Biodistribution and clearance

100 μL of 2.5 μM ^{99m}Tc-labeled QDs (see Supplementary Methods) were administered intravenously into 25 g CD-1 mice (~100 μCi). Mice were housed in special cages to allow for the collection of urine and feces. Measurement of blood clearance was performed by intermittent sampling of the tail vein. Mice were sacrificed 4 h post-injection. To measure total urinary excretion, the ureters and urethra were ligated with silk sutures, and the bladder removed *en masse* and combined with excreted urine, prior to measurement of radioactivity in a dose calibrator. The remaining carcass was also measured in a dose calibrator, then the skin, adipose, muscle, bone, heart, lungs, spleen, liver, kidneys, stomach, intestine, brain, and feces were resected, washed twice in PBS, pH 7.4, weighed, and their radioactivity measured on a Wallac Wizard (model 1470, Perkin Elmer, Wellesley, MA) 10-detector gamma counter. Curve fitting was performed using Prism version 4.0a software (GraphPad, San Diego, CA).

Supplementary Material

Refer to Web version on PubMed Central for supplementary material.

Acknowledgments

The Biophysical Instrumentation Facility for the Study of Complex Macromolecular Systems (NSF-0070319 and NIH GM68762) is gratefully acknowledged. This work was supported in part by NIH grant #R33-EB-000673 (JVF and MGB), NIH grant #R01-CA-115296 (JVF), and a fellowship from the Charles A. King Trust, Bank of America, Co-Trustee (HSC). MGB also acknowledges support from the NIH funded MIT-Harvard NanoMedical Consortium (1U54-CA119349, a Center of Cancer Nanotechnology Excellence).

REFERENCES

1. Frangioni JV. New technologies for human cancer imaging. J Clin Oncol 2008;26:4012–4021. [PubMed: 18711192]
2. Choi HS, et al. Renal clearance of quantum dots. Nat Biotechnol 2007;25:1165–1170. [PubMed: 17891134]

3. Alivisatos P. The use of nanocrystals in biological detection. Nat Biotechnol 2004;22:47–52. [PubMed: 14704706]
4. Gao X, Cui Y, Levenson RM, Chung LW, Nie S. In vivo cancer targeting and imaging with semiconductor quantum dots. Nat Biotechnol 2004;22:969–976. [PubMed: 15258594]
5. Michalet X, et al. Quantum dots for live cells, in vivo imaging, and diagnostics. Science 2005;307:538–544. [PubMed: 15681376]
6. Medintz IL, Uyeda HT, Goldman ER, Mattoussi H. Quantum dot bioconjugates for imaging, labelling and sensing. Nat Mater 2005;4:435–446. [PubMed: 15928695]
7. Harisinghani MG, et al. Noninvasive detection of clinically occult lymph-node metastases in prostate cancer. N Engl J Med 2003;348:2491–2499. [PubMed: 12815134]
8. Frangioni JV. Translating in vivo diagnostics into clinical reality. Nat Biotechnol 2006;24:909–913. [PubMed: 16900127]
9. Colvin V. The potential environmental impact of engineered nanomaterials. Nat Biotechnol 2003;21:1166–1170. [PubMed: 14520401]
10. Duncan R. Polymer conjugates as anticancer nanomedicines. Nat Rev Cancer 2006;6:688–701. [PubMed: 16900224]
11. Weissleder R, Kelly K, Sun EY, Shtatland T, Josephson L. Cell-specific targeting of nanoparticles by multivalent attachment of small molecules. Nat Biotechnol 2005;23:1418–1423. [PubMed: 16244656]
12. Ballou B, et al. Sentinel lymph node imaging using quantum dots in mouse tumor models. Bioconjug Chem 2007;18:389–396. [PubMed: 17263568]
13. Qian X, et al. In vivo tumor targeting and spectroscopic detection with surface-enhanced Raman nanoparticle tags. Nat Biotechnol 2008;26:83–90. [PubMed: 18157119]
14. Peer D, et al. Nanocarriers: Emerging platforms for cancer therapy. Nat Nanotechnol 2007;2:751–760. [PubMed: 18654426]
15. Hamad I, Hunter AC, Szebeni J, Moghimi SM. Poly(ethylene glycol)s generate complement activation products in human serum through increased alternative pathway turnover and a MASP-2-dependent process. Mol Immunol 2008;46:225–232. [PubMed: 18849076]
16. Dobrovolskaia MA, McNeil SE. Immunological properties of engineered nanomaterials. Nat Nanotechnol 2007;2:469–478. [PubMed: 18654343]
17. Yang J, et al. Development of aliphatic biodegradable photoluminescent polymers. Proc Natl Acad Sci U S A 2009;106:10086–10091. [PubMed: 19506254]
18. Barstow L, Small RE. Liver function assessment by drug metabolism. Pharmacotherapy 1990;10:280–288. [PubMed: 2388874]
19. McAfee JG, et al. Technetium-99m DADS complexes as renal function and imaging agents: II. Biological comparison with iodine-131 hippuran. J Nucl Med 1985;26:375–384. [PubMed: 3981257]
20. Cai W, et al. Peptide-labeled near-infrared quantum dots for imaging tumor vasculature in living subjects. Nano Lett 2006;6:669–676. [PubMed: 16608262]
21. Smith AM, Duan H, Mohs AM, Nie S. Bioconjugated quantum dots for in vivo molecular and cellular imaging. Adv Drug Deliv Rev 2008;60:1226–1240. [PubMed: 18495291]
22. Chen K, Li ZB, Wang H, Cai W, Chen X. Dual-modality optical and positron emission tomography imaging of vascular endothelial growth factor receptor on tumor vasculature using quantum dots. Eur J Nucl Med Mol Imaging 2008;35:2235–2244. [PubMed: 18566815]
23. Bentolila LA, Ebenstein Y, Weiss S. Quantum dots for in vivo small-animal imaging. J Nucl Med 2009;50:493–496. [PubMed: 19289434]
24. Matsumura Y, Oda T, Maeda H. General mechanism of intratumor accumulation of macromolecules: advantage of macromolecular therapeutics. Gan To Kagaku Ryoho 1987;14:821–829. [PubMed: 2952066]
25. Humblet V, et al. High-affinity near-infrared fluorescent small-molecule contrast agents for in vivo imaging of prostate-specific membrane antigen. Mol Imaging 2005;4:448–462. [PubMed: 16285907]
26. Chen X, Park R, Shahinian AH, Bading JR, Conti PS. Pharmacokinetics and tumor retention of 125I-labeled RGD peptide are improved by PEGylation. Nucl Med Biol 2004;31:11–19. [PubMed: 14741566]

27. Liu W, et al. Compact cysteine-coated CdSe(ZnCdS) quantum dots for in vivo applications. J Am Chem Soc 2007;129:14530–14531. [PubMed: 17983223]

28. Davis ME, Chen ZG, Shin DM. Nanoparticle therapeutics: an emerging treatment modality for cancer. Nat Rev Drug Discov 2008;7:771–782. [PubMed: 18758474]

29. Choi HS, et al. Tissue- and organ-selective biodistribution of NIR fluorescent quantum dots. Nano Lett 2009;9:2354–2359. [PubMed: 19422261]

30. Tanaka E, Choi HS, Fujii H, Bawendi MG, Frangioni JV. Image-guided oncologic surgery using invisible light: completed pre-clinical development for sentinel lymph node mapping. Ann Surg Oncol 2006;13:1671–1681. [PubMed: 17009138]

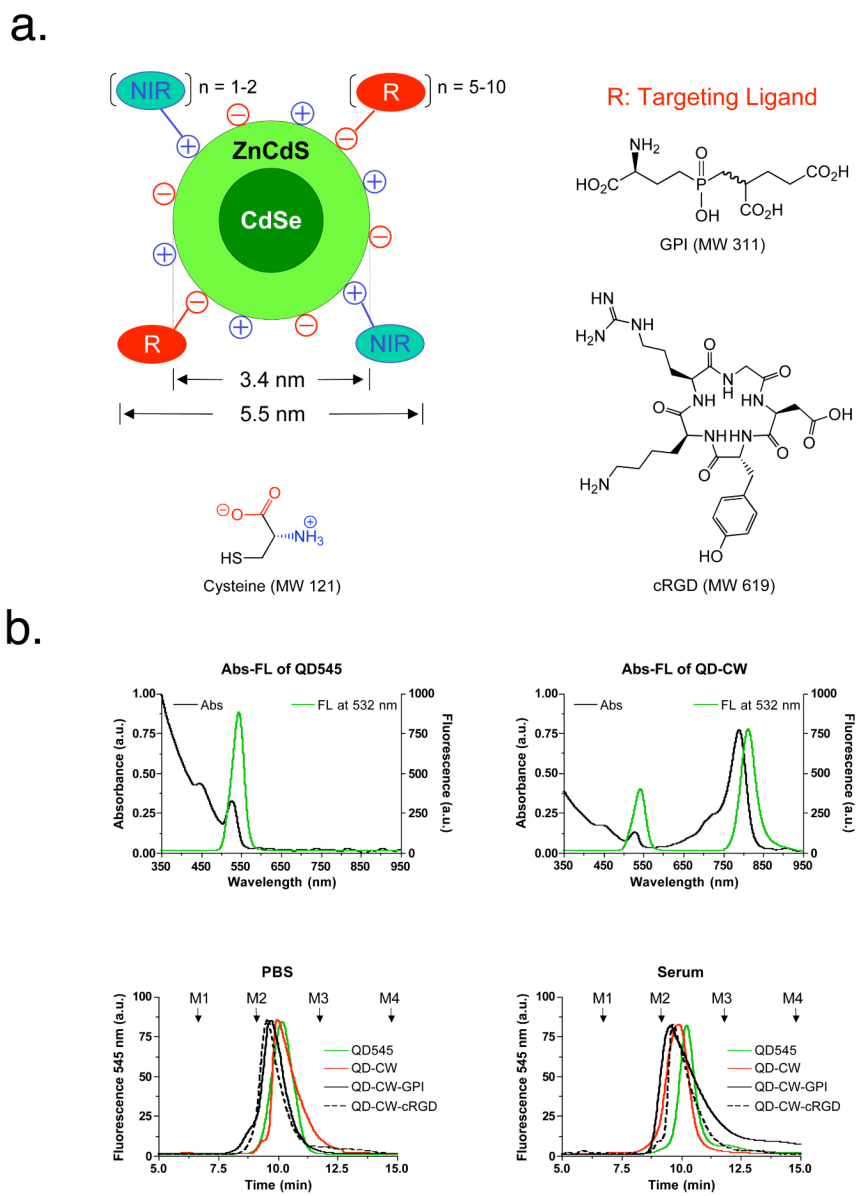

Figure 1.

Design and characterization of nanoparticles. **a**, Chemical conjugation of targeting ligands (R) and NIR fluorophores with cysteine-coated CdSe(ZnCdS) core(shell) QDs. **b**, Absorption (Abs) and fluorescence (FL) emission (λ_{Exc} = 532 nm) spectra (top panels) of QD545 (left) and QD-CW (right). Gel-filtration chromatography (mobile phase = PBS, pH 7.4) analysis (bottom panels) of the different nanoparticles in PBS (left) and after 4 h incubation in 100% mouse serum (right). λ_{Exc} = 532 nm. Molecular weight markers M1 (γ-globulin; 158 kDa, 11.9 nm HD), M2 (ovalbumin; 44 kDa, 6.13 nm HD), M3 (myoglobin; 17 kDa, 3.83 nm HD), and M4 (vitamin B_{12}, 1.35 kDa, 1.48 nm) are shown by arrows.

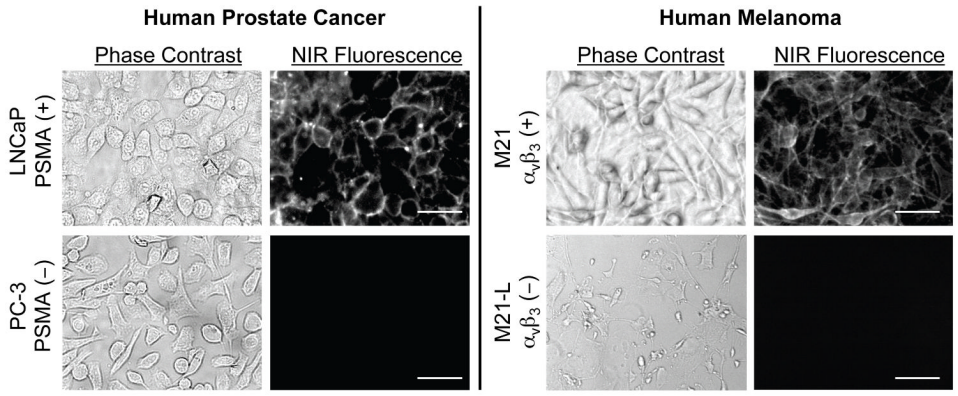

Figure 2.

Live cell binding of targeted QDs *in vitro*: NIR fluorescence imaging of QD-CW-GPI after incubation with PSMA-positive LNCaP and PSMA-negative PC-3 prostate cancer cells (left), and of QD-CW-cRGD after incubation with $\alpha_v\beta_3$-positive M21 and $\alpha_v\beta_3$-negative M21-L melanoma cells (right). For each are shown phase contrast (left) and NIR fluorescence (right) images. Fluorescence images have identical exposure times and normalizations. Scale bar = 10 μm.

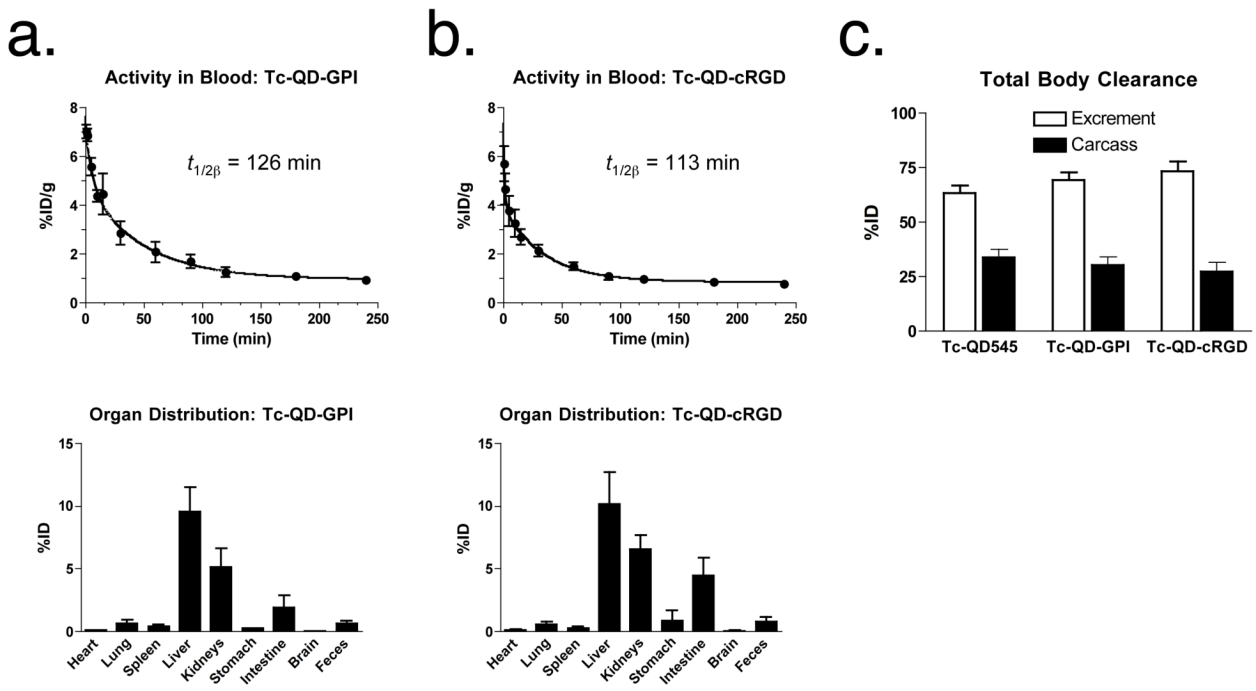

Figure 3.

Total body clearance of targeted nanoparticles 4 h post-intravenous injection into CD-1 mice. Each data point is the mean ± S.D. from n = 4 animals. Blood concentration (%ID/g) and organ distributions (%ID) for ^{99m}Tc-QD-GPI (**a**) and ^{99m}Tc-QD-cRGD (**b**). **c**, Elimination in excrement (white) and retained dose in carcass (black) of ^{99m}Tc-QD545, ^{99m}Tc-QD-GPI, and ^{99m}Tc-QD-cRGD.

a.

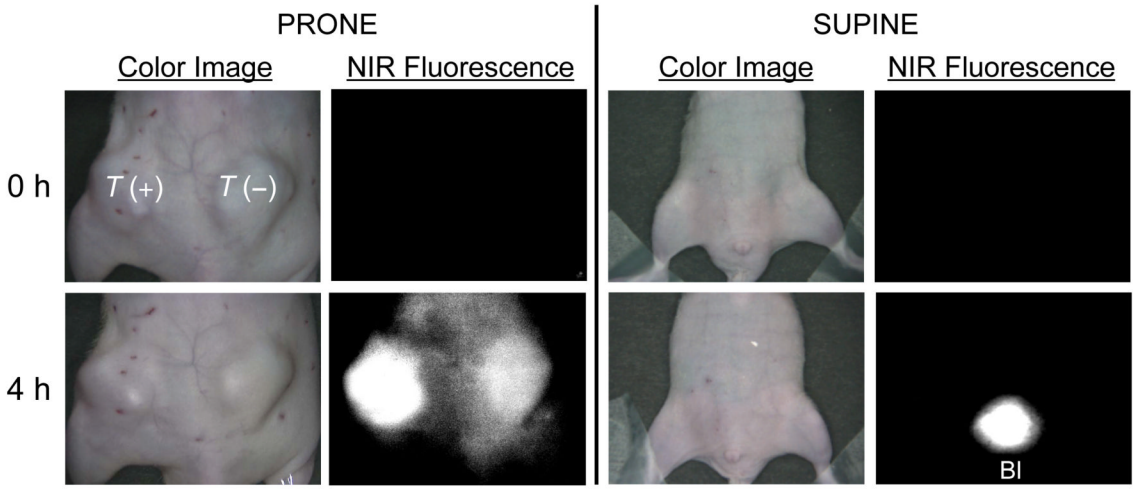

b.

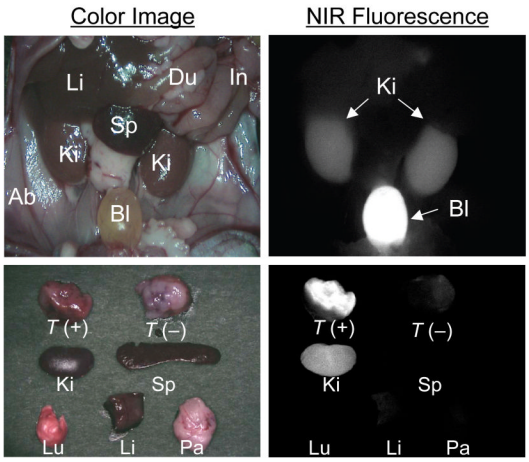

c.

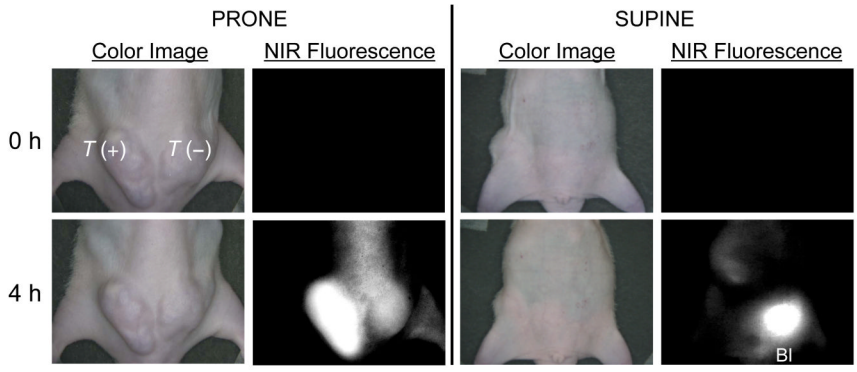

d.

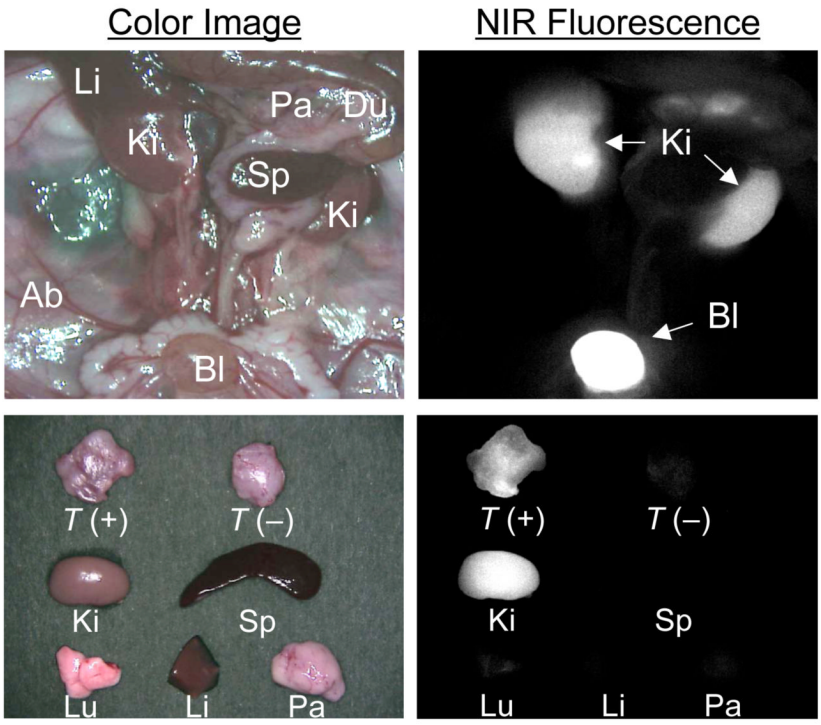

Figure 4.

In vivo fluorescence imaging of human prostate cancer and melanoma xenograft tumors. **a**, 10 pmol/g (0.2 μg/g) of QD-CW-GPI was injected intravenously and observed for 4 h. The PSMA-positive LNCaP tumor (T+) and PSMA-negative PC-3 tumor (T-) are indicated. Shown are representative (n = 5 animals) images of color video (left) and NIR fluorescence (right) for animals in prone (left) or supine (right) position. **b**, *In situ* (top row) and resected (bottom row) organs from (**a**) were imaged 4 h post-injection with color video (left) and NIR fluorescence (right). **c**, 10 pmol/g (0.2 μg/g) of QD-CW-cRGD was injected intravenously and observed for 4 h. The $\alpha_v\beta_3$-positive M21 tumor (T+) and $\alpha_v\beta_3$-negative M21-L tumor (T-) are indicated. Shown are representative (n = 5 animals) images of color video (left) and NIR fluorescence (right) for animals in prone (left) or supine (right) position. **d**, *In situ* (top row) and resected (bottom row) organs from (**c**) were imaged 4 h post-injection with color video (left) and NIR fluorescence (right). Ki, kidneys; Du, duodenum; Sp, spleen; In, intestine; Lu, lungs; Li, liver; Pa, pancreas; Ab, abdominal wall; and Bl, bladder.

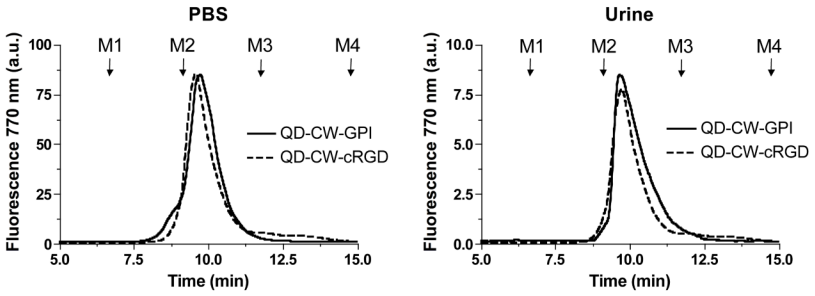

Figure 5.

HD measurements of renally excreted QDs: QD-CW-GPI (solid curve) and QD-CW-cRGD (dotted curve) in PBS (left) and in urine collected 4 h post-injection (right). λ_{Exc} = 770 nm. Molecular weight markers (arrows) are as described in Fig. **1b**.